

1 Surface predictor of overturning circulation and heat content change in 2 the subpolar North Atlantic

3
4 Damien. G. Desbruyères*¹ ; Herlé Mercier² ; Guillaume Maze¹ ; Nathalie Daniault²

5
6 1. Ifremer, University of Brest, CNRS, IRD, Laboratoire d’Océanographie Physique et
7 Spatiale, IUEM, Ifremer centre de Bretagne, Plouzané, 29280, France

8
9 2. University of Brest, CNRS, Ifremer, IRD, Laboratoire d’Océanographie Physique et
10 Spatiale, IUEM, Ifremer centre de Bretagne, Plouzané, 29280, France

11 Corresponding author: Damien Desbruyères (damien.desbruyeres@ifremer.fr)

12
13 **Abstract.** The Atlantic Meridional Overturning Circulation (AMOC) impacts ocean and atmosphere
14 temperatures on a wide range of temporal and spatial scales. Here we use observational data sets to
15 validate model-based inferences on the usefulness of thermodynamics theory in reconstructing AMOC
16 variability at low-frequency, and further build on this reconstruction to provide prediction of the near-
17 future (2019-2022) North Atlantic state. An easily-observed surface quantity – the rate of warm to cold
18 transformation of water masses at high latitudes – is found to lead the observed AMOC at 45°N by 5-6
19 years and to drive its 1993-2010 decline and its ongoing recovery, with suggestive prediction of extreme
20 intensities for the early 2020’s. We further demonstrate that AMOC variability drove a bi-decadal
21 warming-to-cooling reversal in the subpolar North Atlantic before triggering a recent return to warming
22 conditions that should prevail at least until 2021. Overall, this mechanistic approach of AMOC variability
23 and its impact on ocean temperature brings new keys for understanding and predicting climatic conditions
24 in the North Atlantic and beyond.

25 1. Introduction

26 The north-eastward meandering flow of the North Atlantic Current (NAC) dominates the upper-ocean

27 circulation of the northern North Atlantic (Krauss, 1986). It transports relatively warm waters that release
28 heat to the atmosphere as they flow around the Subpolar Gyre (SPG) and the Nordic Seas, ultimately
29 forming North Atlantic Deep Water that propagates in the deep layers via upper and deep western
30 boundary currents (DWBC) and dispersive interior pathways (Bower et al., 2009; Lherminier et al., 2010,
31 see Figure S1 for domain boundaries and bathymetric features). On top of sequestering physical and
32 biogeochemical properties in the deep seas, the warm-to-cold conversion of water masses and the
33 meridional overturning circulation associated with it drives a significant meridional heat transport. Its
34 variability is thought to be a major cause of temperature and ocean heat content (OHC) shifts in the upper
35 layer of the northern North Atlantic, with important ramification for ocean-atmosphere interactions and
36 large-scale climate variability (Bryden et al., 2014; Robson et al., 2017). In particular, the most recent
37 reversal of climatic trends in the north Atlantic SPG since 2005 (warming to cooling) has been attributed
38 in numerical models to a decadal weakening of the ocean meridional heat transport across the southern
39 boundary of the SPG (Piecuch et al., 2017; Robson et al., 2016). The recent return of intense ocean-to-
40 atmosphere heat loss (and associated deep convection) since the mid 2010's (Josey et al., 2018;
41 Yashayaev and Loder, 2017) is now suggestive of an ongoing or approaching re-intensification of the
42 circulation and, consequently, a shift to warming condition in the SPG. Overall, the need for a continuous
43 monitoring of the top-to-bottom current field in the SPG has appeared critical to capture the many
44 components of this warm-to-cold transformation. In 2014, international efforts led to the implementation
45 of an in situ mooring array aimed to fulfil such a need – the Overturning in the Subpolar North Atlantic
46 Program (OSNAP; Lozier et al., 2017).

47 In the commonly-used depth space (z), the $AMOC_z$ streamfunction helps to simplify the complex three-
48 dimensional velocity field of the North Atlantic into a northward flow of *about* 16 Sv ($1 \text{ Sv} = 10^6 \text{ m}^3 \text{ s}^{-1}$)
49 in the upper 0-1000 m or so and a compensating southward flow at depth, connected vertically by the net
50 sinking of surface waters at high latitudes (Buckley and Marshall, 2016; Wunsch, 2002). However, if one
51 is interested in OHC and the dynamics of buoyancy redistribution in the ocean, an estimator of the
52 circulation in density-space (σ) must be preferred, which we will note $AMOC_\sigma$ hereafter. Such an
53 estimator allows to fully capture transformation of light water masses into denser ones at high latitudes,

54 along both the vertical overturning and horizontal gyre circulations (Lherminier et al., 2010; Pickart and
55 Spall, 2007).

56 In the absence of diapycnal mixing, the diapycnal volume fluxes associated with the $AMOC_{\sigma}$ at a given
57 latitude must relate to air-sea exchanges of buoyancy within isopycnal outcrops north of this latitude
58 (Figure 1). This thermodynamic balance between the $AMOC_{\sigma}$ and its surface-forced component (noted
59 $SFOC_{\sigma}$ hereafter), theorized by Walin (1982) and much later verified with numerical models (Grist et al.,
60 2010; Marsh, 2000), suggests key monitoring and predictive skill of $AMOC_{\sigma}$. This was particularly
61 evidenced in low-resolution coupled climate models, which hold a significant lagged relationship between
62 high latitude surface forcing and overturning circulation at the southern exit of the SPG (Grist et al.,
63 2009). In a follow-up paper, Grist et al. (2014) estimated the surface-forced component of the AMOC in
64 several atmospheric reanalyses and highlighted their overall consistency in the SPG. An independent
65 validation of those surface indices with observation-based time series of the interior circulation is
66 however, still missing. Moreover, the potential of such proxy-based reconstruction of the AMOC for
67 predicting OHC variability and new climatic reversal in the coming years remains to be shown.

68 The primary purposes of the present study are (1) to validate with observational data the predictive skill
69 of surface-forced water mass transformation for AMOC variability, and (2) to assess the causal link
70 between AMOC variability and decadal OHC changes in the SPG and perform near-future prediction of
71 those quantities. Regional variability will also be documented, with details on the capability of the *in situ*
72 OSNAP array in monitoring the basin-wide $AMOC_{\sigma}$.

73 The paper is structured as follows. Section 2 presents the observational data sets and the methodology
74 used to compute $AMOC_{\sigma}$, $SFOC_{\sigma}$, and OHC. Section 3 gathers the main results of the study and Section
75 4 summarizes and discusses them.

77 **2.1. Data**

78 Monthly gridded potential temperature (θ) and practical salinity (S) profiles from four *in situ*
79 hydrographic datasets were used. Details on those data sets (EN4, CORA, ISHII and ARMOR3D) are
80 provide in Table S1. For each product and at each grid point, the θ and S profiles were interpolated to a
81 regular 20 db vertical spacing. Using the TEOS-10 Gibbs-SeaWater (GSW) toolbox, practical salinity
82 was converted to absolute salinity, potential temperature to conservative temperature, and σ_0 and σ_1
83 (potential density relative to sea-surface and 1000 m, respectively) were computed. Air-sea heat fluxes
84 (radiative and turbulent) and freshwater fluxes (evaporation and precipitation) are obtained from three
85 atmospheric reanalyses (NCEP2, ERA-I and CERES, see Table S1). Absolute dynamic topography and
86 associated surface meridional geostrophic velocities are obtained from the AVISO platform
87 (<https://www.aviso.altimetry.fr/en/data.html>) and combine sea-level anomalies from multi-mission
88 satellite altimeters and mean dynamic topography from GOCE, GRACE, altimetry and in situ data
89 (<https://www.aviso.altimetry.fr/en/data/products/auxiliary-products/mdt.html>).

90 The various integrated quantities derived from those data products (such as ocean heat content of
91 overturning stream functions - see description below in Section 2.2 and 2.3) were then combined into
92 ensemble mean over the period (1993-2017 for altimetry-related quantities, 1985-2017 otherwise), with
93 associated ensemble standard errors computed as $\frac{\sigma}{\sqrt{N-1}}$, where σ is the standard deviation and $N = 4$ the
94 number of data products used in the mean. This error captures the spread induced by the different methods
95 used as of today to interpolate sparse in situ observations. Further notes on statistical analysis of the
96 reported results (correlation, trend error) are provided in Supplementary Information.

97 **2.2. Computation of AMOC_σ , MHT_σ and associated OHC**

98 The 0-2000 m absolute meridional velocities v at 45°N are derived by referencing *in situ* estimates of the
99 geostrophic thermal-wind currents with altimetry-derived sea-surface geostrophic velocities, following
100 previously-published methodologies (Gourcuff et al., 2011; Mercier et al., 2015; Sarafanov et al., 2012).

101 The latitude 45°N represents the southern geographic boundary of the SPG with the bulk of the light-to-
 102 dense transformation associated with the $AMOC_{\sigma}$ occurring north of it (see Section 3.1). Moreover, the
 103 thermohaline fronts (and the resulting relative velocities) at 45°N are relatively well defined in ocean
 104 analysis products due to good data coverage, notably at the western boundary. This latitudinal band is
 105 therefore chosen as our reference line for computing a realistic $AMOC_{\sigma}$ and undertaking its subsequent
 106 mechanistic analysis.

107

108 The $AMOC_{\sigma}$ stream function is obtained by integrating v zonally and vertically above each σ_1 surface
 109 (spaced by $\delta\sigma = 0.025 \text{ kg m}^{-3}$). The maximum value of the resulting stream function at the density level
 110 σ_m writes as:

$$111 \quad AMOC_{\sigma_m} = \int_x \int_{\sigma < \sigma_m} v dx dz$$

112

113 We restrict such calculation to the 0-2000 m layer as not all products contain data below that depth¹. This
 114 threshold is nonetheless deep enough to capture the level of maximum transformation at 45°N, as well as
 115 its variability. The $AMOC_{\sigma}$ -driven heat transport is estimated as in Mercier et al. (2015):

116

$$117 \quad MHT_{\sigma} = \rho_0 C_p AMOC_{\sigma_m} \Delta \theta$$

118

119 where $\rho_0 = 1025 \text{ kg m}^{-3}$, $C_p = 4000 \text{ J kg}^{-1} \text{ }^{\circ}\text{C}^{-1}$ and $\Delta \theta$ is the temperature difference between the upper
 120 and lower limbs of the $AMOC_{\sigma}$ (i.e. the area-weighted average temperature of water lighter than σ_m minus
 121 the area-weighted average temperature of water heavier than σ_m). Note that $\Delta \theta$ was computed from the
 122 EN4.2.0 product that provides full-depth temperature profiles. The change in ocean heat content north of
 123 45°N driven by MHT_{σ} is then estimated as:

¹ This is due to the fact that the main source of recent in situ data is the Argo array of profiling floats (Riser et al., 2016) providing quality controlled temperature and salinity data for the upper 2000m only.

124
$$OHC(t)_{MHT\sigma} = \int_{t_0}^t (MHT(t)_\sigma - \overline{MHT}_\sigma) dt$$

125 where t is a given year and the overbar refers to a temporal average over the period 1996 – 2013. This
 126 reference period is assumed to represent a climatological equilibrium state around which
 127 MHT_σ fluctuates, so that positive (negative) anomalies in MHT_σ result in warming (cooling) north of
 128 45°N. As shown in Section 3.3, this assumption yields high and significant correlation between
 129 $OHC_{MHT\sigma}$ and the observed OHC in the SPG.

130

131 **2.3. Computation of SFOC $_\sigma$.**

132 The surface-forced component of the overturning streamfunction SFOC $_\sigma$ was computed following
 133 common practice and methodologies (Marsh, 2000). For each month and each isopycnal σ (spaced by $\delta\sigma$
 134 = 0.05 kg m $^{-3}$), SFOC $_\sigma$ is computed as the diapycnal convergence of the diapycnal volume flux driven by
 135 surface density flux wherever σ outcrops north of a given coast-to-coast section:

136

137
$$SFOC(\sigma^*) = \frac{1}{\delta\sigma} \iint \left[-\frac{\alpha Q}{C_p} + \beta \frac{S}{1-S} (E - P) \right] \Pi(\sigma) dx dy$$

138 where

139
$$\Pi(\sigma) = \begin{cases} 1 & \text{for } \sigma - \frac{\delta\sigma}{2} < \sigma < \sigma + \frac{\delta\sigma}{2} \\ 0 & \text{elsewhere} \end{cases}$$

140

141 The quantity within brackets is the local surface density flux, α and β are the thermal expansion and
 142 haline contraction coefficients, C_p is specific heat capacity of sea water (4000 J kg $^{-1}$ K $^{-1}$), Q the net
 143 surface heat flux, E the evaporation rate, and P the precipitation rate. Following Marsh (2000), monthly
 144 fields of surface temperature (for density computation) and Q are used herein while monthly climatology
 145 values for surface salinity S and $E - P$ are used to avoid introducing punctual spurious surface density
 146 anomalies due to poor salinity sampling (especially in the early historical record), notably near continental
 147 margin and seasonally-covered ice-covered areas. We note here that the air-sea buoyancy flux in the SPG,

148 and therefore $SFOC_{\sigma}$, is largely controlled by its thermal component (Marsh, 2000). When for a given
 149 month (usually during summer), σ does not outcrop north of 45°N , $SFOC_{\sigma}$ is set to zero. Annual averages
 150 are then obtained for 1985-2017. Even if $SFOC_{\sigma}$ is a surface integral statement, maps of transformation
 151 rates can be obtained by accumulating the integrand over outcrops (Brambilla et al., 2008; Maze et al.,
 152 2009), as shown later in Section 3.1.

153

154 In order to directly relate $SFOC_{\sigma}$ and $AMOC_{\sigma}$, we rely on the assumption of water mass steadiness in the
 155 SPG, meaning that the net accumulation of volume within isopycnal layers is considered to be negligible
 156 in front of the import of light water to be transformed and the export of dense water after transformation
 157 (Marsh, 2000). To verify this hypothesis, we compute $\frac{dV_{\sigma}}{dt}$, the yearly local change in the volume of
 158 discrete isopycnal layer (in Sv), where V_{σ} is evaluated on January 1st of each year. Averaging this term
 159 north of 45°N and summing below the density level of maximum $SFOC_{\sigma}$ yields an evaluation of water
 160 mass steadiness during each year. As discussed later, this term can be intermittently important but does
 161 not dominate the decadal variability, so that a direct link emerges between $SFOC_{\sigma}$ and $AMOC_{\sigma}$ on those
 162 relatively long-time scales.

163

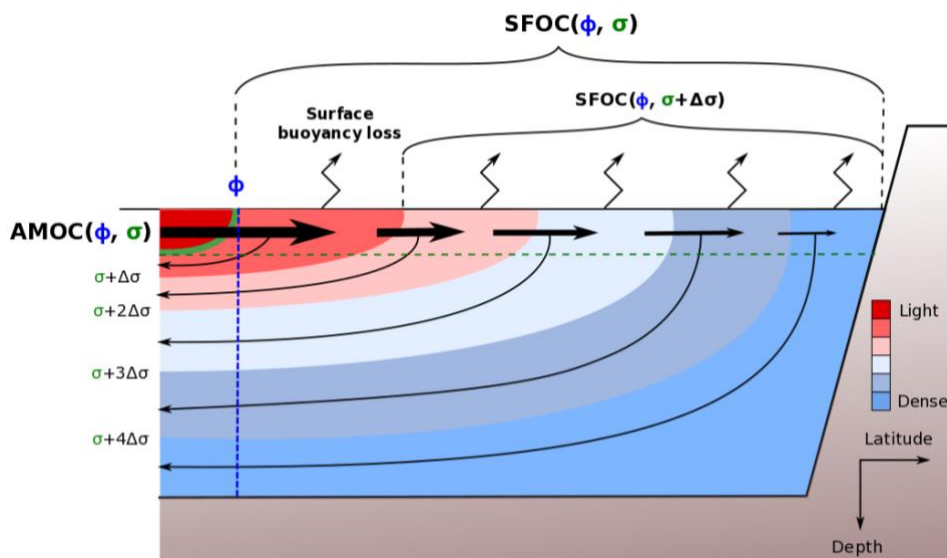


Figure 1. Schematic of the relationship between meridional overturning circulation at latitude ϕ and isopycnal surface σ – the $\text{AMOC}(\phi, \sigma)$ – and its surface-forced component – the $\text{SFOC}(\phi, \sigma)$. Arrows show the progressive transformation of waters across increasing density surfaces balanced by buoyancy loss at the air-sea interface and meridional import and export. After Marsh (2000).

164

165 **3. Results**

166 **3.1. The time-mean AMOC_σ and SFOC_σ**

167 The time-mean depth-longitude field of meridional velocity at 45°N (Figure 2A) is dominated by a
168 western boundary current system in good quantitative agreement with direct current estimates carried out
169 in the region (Mertens et al., 2014; Toole et al., 2017). This current system includes the southward-
170 flowing Labrador Current (LC) adjacent to the slope above 800 m (16 Sv), the upper part of the
171 southward-flowing DWBC circa 47°W with increasing velocities with depth (13 Sv), and the surface-
172 intensified northward-flowing NAC (53 Sv) with its recirculation east of 45°W (28 Sv). Meridional
173 velocities are significantly weaker further east in the gyre interior. Integrating zonally the volume
174 transport above discrete σ_1 -surfaces yields the (partial) AMOC_σ stream function at 45°N , which reaches
175 a time-mean maximum value of 14.3 ± 1.4 Sv at $\sigma_1 = 32.15$ (Figure 2B; see also Figure S2A for the
176 AMOC_σ stream function of each individual product). A similar calculation in depth space yields the
177 (partial) AMOC_z stream function at 45°N , which reaches a time-mean maximum value of 9 ± 0.4 Sv at
178 700 m depth (Figure S2B). Therefore, about 60% of the maximum diapycnal volume flux above 2000 m
179 depth at 45°N is associated with a net downwelling in the vertical plane, the remainder being due to dense

180 waters returning at the same depth as that of the inflowing light waters within the horizontal gyre
 181 circulation.

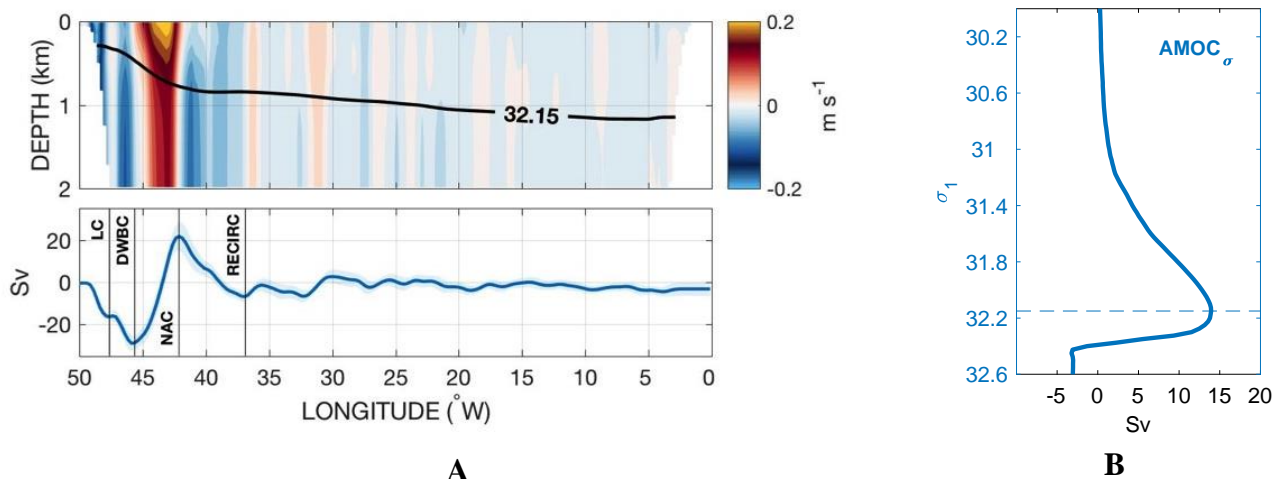


Figure 2. Meridional velocity and transport at 45°N ($AMOC_{\sigma}$). (A) Top: The 1993-2017 mean longitude-depth velocity field (in $m s^{-1}$) at 45°N. The $\sigma_1 = 32.15$ isopycnal across which the maximum diapycnal flux occurs is shown in black. Bottom: The depth-integrated (0-2000 m) zonally cumulated transport (in Sv) at 45°N, with labels as follow: LC (Labrador Current), DWBC (Deep Western Boundary Current), NAC (North Atlantic Current) and RECIRC (NAC recirculation). Shading indicates the ensemble standard error. (B). The mean $AMOC_{\sigma}$ streamfunction at 45°N (in Sv). Shading indicates the ensemble standard error. The blue dashed line at $\sigma_1 = 32.15$ depicts the maximum transformation rate.

182 The surface-forced component of the $AMOC_{\sigma}$ (noted $SFOC_{\sigma}$) shows a maximum time-mean value of
 183 15.4 ± 1.8 Sv at $\sigma_0 = 27.4$ (or $\sigma_1 \approx 32$), which reflects a light-to-dense flux that primarily occurs along the
 184 NAC path in the eastern SPG south of Reykjanes Ridge and to a lesser extent along the western SPG
 185 boundary (Labrador Sea), along the Norwegian margins (Figure 3). This pattern is consistent with recent
 186 mooring-based analysis of the diapycnal overturning in the SPG showing a relatively minor contribution
 187 of the Labrador Sea to the basin-wide maximum transformation rates (Lozier et al., 2019). This is because
 188 the density level of maximum transformation in the Labrador Sea is well below the density level of the
 189 basin-wide $AMOC_{\sigma}$ (or $SFOC_{\sigma}$). The spatial distribution of the surface-forced diapycnal volume flux
 190 within the domain is inferred by evaluating $SFOC_{\sigma}$ at two additional key sections: the international
 191 Canada-Greenland-Scotland OSNAP and the Greenland-Iceland-Scotland (GIS) sills. The $SFOC_{\sigma}^{OSNAP}$

192 and $\text{SFOC}_\sigma^{\text{GIS}}$ stream functions respectively show a maximum transformation rate of $11.2 \pm 1.3 \text{ Sv}$ at σ_0
 193 $= 27.52$ and $5.4 \text{ Sv} \pm 0.4 \text{ Sv}$ at $\sigma_0 = 27.77$, in good agreement with independent *in situ* calculations of the
 194 maximum overturning across the OSNAP line and overflow transport estimates at the GIS (Hansen and
 195 Østerhus, 2000; Li et al., 2017). Altogether, the three estimates of SFOC_σ across 45°N , OSNAP, and GIS,
 196 describe the expected decrease in intensity and increase in density of the maximum transformation rate
 197 as one progress northward. We note that the density level of the maximum SFOC_σ at 45°N is slightly
 198 lighter than the density level of the maximum AMOC_σ at 45°N . This is because SFOC_σ cannot account
 199 for the positive transformation rate due to the entrainment-driven mixing of the subpolar mode waters
 200 with the denser overflow waters in the vicinity of the GIS sills. However, the analysis of numerical
 201 simulations shows that such a mixing contribution does not largely affect interannual and decadal
 202 variability (Marsh et al., 2005), our primary purpose here.

203

204

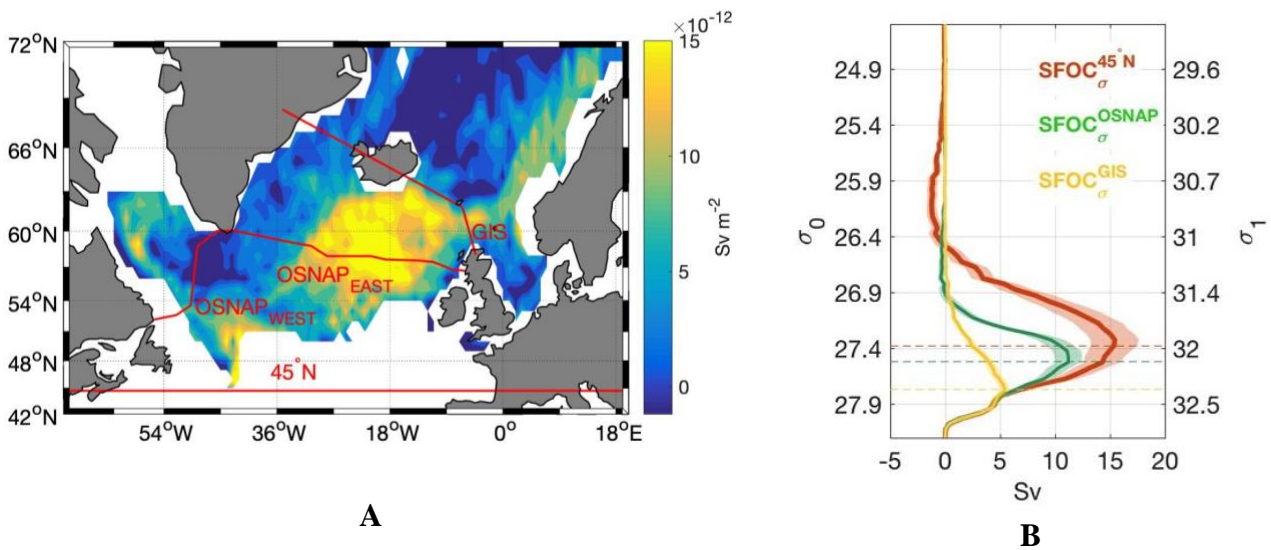


Figure 3. The surface-forced transformation north of 45°N (SFOC_σ). (A) The 1993-2017 time-mean transformation map across the isopycnal surface $\sigma_0 = 27.4$ (in Sv m^{-2}), across which the maximum transformation rate north of 45°N occurs. (B) The mean SFOC_σ streamfunction (in Sv) at 45°N (red), at the OSNAP line (green) and at the GIS sills (yellow). See 5A) for section locations. Shading indicates the ensemble standard error. The dashed lines depict the density levels of maximum surface-forced transformation rate north for each domain. As the computation was made using σ_0 , the corresponding surface σ_1 values are shown on the

right-hand side y-axis. The surface integral of the diapycnal volume flux shown in (A) yields the maximum transformation rate through $\sigma_0 = 27.4 : 15.4 \pm 1.8$ Sv.

205

206 **3.2. The variability of $AMOC_\sigma$ and $SFOC_\sigma$**

207 The maximum $AMOC_\sigma$ time series, displayed as raw and 7-year low-pass filtered annual anomalies in
208 Figure 4A (blue lines), shows an apparent 8-year period variability embedded in a linear decrease during
209 1993-2010 of -0.24 ± 0.05 Sv yr⁻¹ and a subsequent intensification during 2010-2017 of 0.91 ± 0.19 Sv
210 yr⁻¹. Those changes are largely advective (Figure S4), indicating minor impact of volume (or σ_m)
211 variability on the AMOC intensity. Volume redistribution associated with the formation history of
212 intermediate water masses in the Labrador and Irminger seas can be important but they remain restricted
213 to the lower limb of the $AMOC_\sigma$ (not shown). We note that the $AMOC_z$ shares a similar variability with
214 $AMOC_\sigma$ but of weaker amplitude, indicating an important contribution of the horizontal circulation
215 (versus vertical overturning) to the diapycnal volume flux variability at 45°N (Figure S4). The gyre
216 contribution to $AMOC_\sigma$ variability at 45°N is also inferred from an independent mooring-based
217 observation of the (400m-bottom) DWBC intensity at 53°N (Zantopp et al., 2017). Although the shortness
218 of the time series (10 years) only allows a suggestive independent validation, the DWBC variability is
219 found to consistently lead the 2004-2010 weakening and the 2010-2014 intensification of the $AMOC_\sigma$ at
220 45°N by 3 years (Figure S4).

221

222 The second independent validation of $AMOC_\sigma$ bears the mechanistic explanation of its variability. While
223 the maximums of $AMOC_\sigma$ and $SFOC_\sigma$ hardly correlate at high frequency, a striking correspondence
224 between their low-pass filtered variability is found, with the largest correlation obtained when the former
225 lags the latter by 5-6 years (0.94 at the 99% confidence level), in line with typical advective time scales
226 in the SPG (Bersch et al., 2007) (Figure 4A – see also Supplementary Materials for details on smoothing
227 and correlation). Therefore, observational data confirm that surface-forced water mass transformation
228 represents a dominant driver as well as an easily-derived proxy of low-frequency $AMOC_\sigma$ changes across

229 the southern exit of the SPG. Departure from an exact match between $AMOC_{\sigma}$ and $SFOC_{\sigma}$ relate to the
 230 influence of the remaining terms in the volume budget equation, namely diapycnal mixing and volume
 231 storage within the SPG interior. As shown in Figure S5, the latter can be non-negligible on interannual
 232 time scale but exhibits minor decadal variability.

233

234 The 5-year time lag between $AMOC_{\sigma}$ and $SFOC_{\sigma}$ time series enables prediction of near-future $AMOC_{\sigma}$
 235 variability. Here, the low-frequency strengthening of the meridional circulation observed since 2010 is
 236 found to continue at a similar rate until 2022 while reaching extreme intensities in 2019 and 2020 similar
 237 to those observed in the early 1990's. Those extreme events reflect harsh atmospheric winter conditions
 238 in the SPG in 2014 and 2015 (North Atlantic Oscillation strongly positive) associated with large ocean-
 239 to-atmosphere heat transfer (Josey et al., 2018). As discussed in the next section, this most recent positive
 240 trend in $AMOC_{\sigma}$ intensity and its predicted persistence until the early 2020's may substantially increase
 241 OHC in the SPG in the coming years.

242

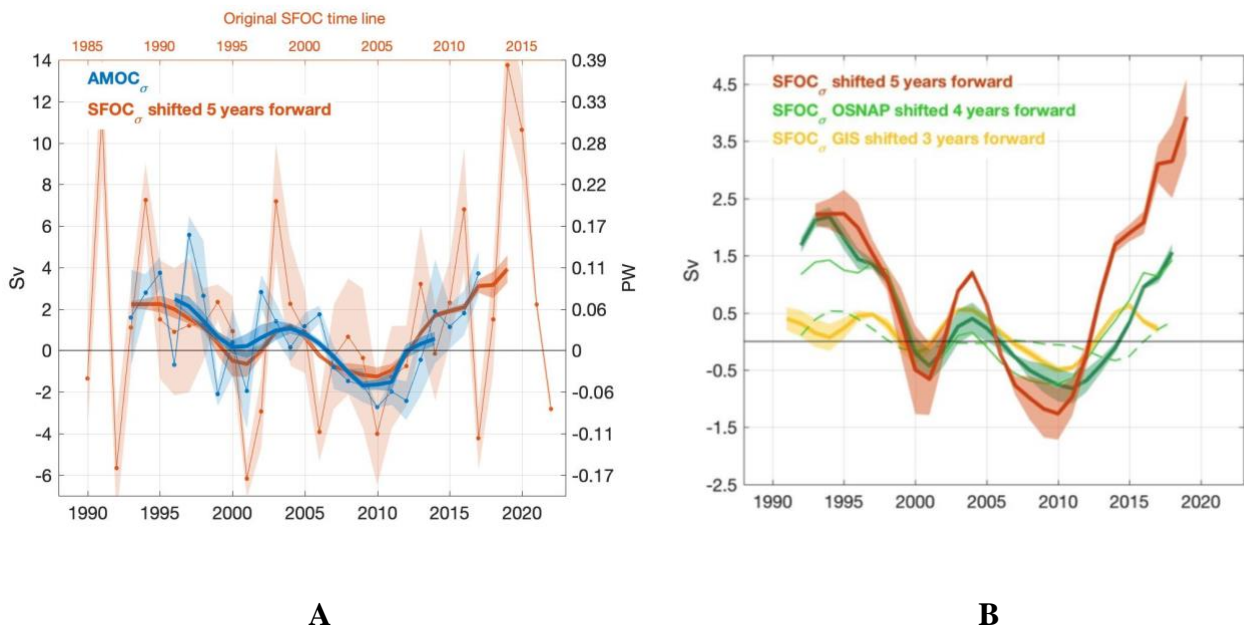


Figure 4. The $AMOC_{\sigma}$ and $SFOC_{\sigma}$. (A) Annual anomalies in the maximum $AMOC_{\sigma}$ (blue) and the maximum $SFOC_{\sigma}$ (red) at 45°N (in Sv), with the latter shifted 5 years forward (lag of maximum correlation). The reference (time-mean) period is 1996-2013. Thick lines show 7-year low-pass filtered time series. The right-hand side axis

displays the corresponding heat transport anomalies. The original time line for $SFOC_{\sigma}$ is given in the top x-axis.

(B) The 7-year low-pass filtered time series of anomalies in the maximum $SFOC_{\sigma}$ at 45°N (red – shifted 5 years forward), the maximum $SFOC_{\sigma}$ at the OSNAP line (green – shifted 4 years forward) decomposed into contributions from the eastern (thin) and western (dashed) basins, and the maximum $SFOC_{\sigma}$ at the GIS sills (yellow – shifted 3 years forward). Shading indicates the ensemble standard errors for each variable.

243

244 The decadal variability in the maximum $SFOC_{\sigma}$ at 45°N has minor contribution from the Nordic Seas and
245 is effectively captured by $SFOC_{\sigma}^{\text{OSNAP}}$, although the contribution from regions south of the OSNAP line
246 appears important during its most recent intensification since 2010 (Figure 4B). The variability in $SFOC_{\sigma}$
247 is dominated by changes in the rate of water mass transformation in the eastern SPG basins, in line with
248 recent mooring-based estimates of the $AMOC_{\sigma}$ across the OSNAP line (Lozier et al., 2019). The
249 successive 1-year lag between $SFOC_{\sigma}$ at 45°N , $SFOC_{\sigma}$ at OSNAP and $SFOC_{\sigma}$ at GIS reflects the
250 progressive northward spreading of transformation anomalies across surface of increasing density (see
251 Figure 3B).

252

253 **3.3. The variability of OHC and its 5-year prediction**

254 The lagged correlation between surface-forced water mass transformation and the overturning circulation
255 has important ramifications for the monitoring of past, present and future fluctuations of $AMOC_{\sigma}$ but
256 does not inform on its role in driving decadal OHC variability in the SPG. To infer such a role, the
257 $AMOC_{\sigma}$ -driven meridional heat transport at 45°N – noted MHT_{σ} hereafter – is computed from the
258 maximum $AMOC_{\sigma}$ index (Figure 4A) and the temperature difference between the upper and lower
259 $AMOC_{\sigma}$ limbs at 45°N (see Section 2.2). The time-mean MHT_{σ} at 45°N during 1993-2017 reaches 0.43
260 ± 0.04 PW and is balanced by an ocean-to-atmosphere heat transfer of 0.21 ± 0.04 PW, a small long-term
261 change in OHC within the SPG domain of 0.014 ± 0.002 PW, and a northward ocean heat transport across
262 the GIS sills estimated as a residual as 0.20 PW (consistent with independent estimates, Curry et al., 2011;
263 Hansen et al., 2015; Hansen & Østerhus, 2000).

265 The cumulated anomalies of MHT_{σ} referenced to the time-window 1996-2013 show high correlation with
 266 the observed OHC within the 0-1000 m layer of the SPG ($10^{\circ}W-70^{\circ}W$; $45^{\circ}N-65^{\circ}N$, Figure 5). In
 267 particular, both the 1993-2006 warming and the 2006-2013 cooling of the region are well explained by
 268 the contribution of MHT_{σ} variability at $45^{\circ}N$ ($r = 0.87$ at the 99% confidence level for 1993-2013). This
 269 is consistent with previous model-based inferences that the $AMOC_{\sigma}$ is a primary driver of decadal
 270 temperature changes in the upper SPG (Desbruyères et al., 2015; Grist et al., 2010; Robson et al., 2016).
 271 This causal relationship is however not verified during 2013-2015, where MHT_{σ} induces a warming of
 272 the SPG whereas *in situ* observations indicate that OHC continued to decrease. This apparent discrepancy
 273 reflects the strong air-sea heat flux anomaly that drove a sharp cooling of the upper SPG during those
 274 years – the so-called “Cold blob” (Duchez et al., 2016; Josey et al., 2018). From 2015, atmospheric
 275 conditions were back to “normal” and the MHT_{σ} -driven warming of the SPG could begin.

276

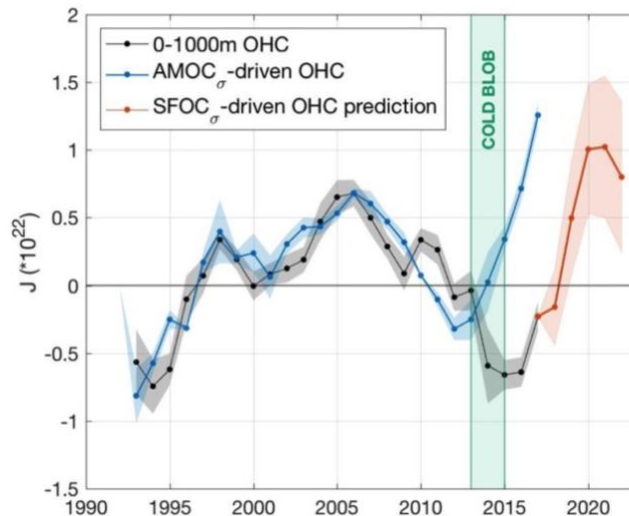


Figure 5. OHC variability. Detrended anomalies in OHC within the upper SPG (0-1000 m; $10^{\circ}W-70^{\circ}W$; $45^{\circ}N-65^{\circ}N$, black, in J) and MHT_{σ} -driven OHC anomalies north of $45^{\circ}N$ (blue, in J). Shading indicates the ensemble standard errors for each variable. The $SFOC_{\sigma}$ -driven OHC prediction for 2017-2022 is shown in red, with its associated error based on the historical predictive skills of $SFOC_{\sigma}$. The green patch indicates the “cold blob” era driven by extreme air-sea flux events (Josey et al., 2018).

277

278 We finally make use of the remarkable 5-year lead of $SFOC_{\sigma}$ onto $AMOC_{\sigma}$ (Figure 4A) to make a
 279 suggestive prediction of $AMOC_{\sigma}$ -driven OHC changes between 2017 and 2022. Annually-averaged
 280 anomalies of $SFOC_{\sigma}$ are scaled by the actual interannual variance of $AMOC_{\sigma}$ and converted into an
 281 anomalous heat transport relative to 1996-2013 with associated OHC anomalies as previously shown. To
 282 make the prediction, we simply anchor the resulting 2017-2022 time series to the last observed OHC
 283 value of 2017 (red line, Figure 5). An uncertainty is added on the prediction based on the skill of $SFOC_{\sigma}$
 284 in predicting the historical 1993-2017 OHC (red shading in Figure 5). This uncertainty is the prediction
 285 error ϵ_{lag} from the N_{lag} -year time series, with $lag = 1$ to 5 years:

286

$$287 \quad \epsilon_{lag} = \sqrt{\frac{1}{N_{lag}} \sum \{(OHC^{y+lag} - OHC^y) - (OHC_{SFOC_{\sigma}}^{y+lag} - (OHC_{SFOC_{\sigma}})^y)\}^2}$$

288

289 Owing to the ongoing intensification of the $AMOC_{\sigma}$ and its presumed persistence until 2019/2020 (Figure
 290 4A), and under the (hypothesized) absence of extreme air-sea heat flux events in the near-future, the
 291 present analysis predicts a rapid OHC surge of $1.03 \pm 0.57 \cdot 10^{22}$ J between 2017 and 2021 (Figure 5).

292

293 **4. Conclusions**

294 In this paper we have provided observationally-based evidence of a tight causal relationship between low
 295 frequency changes in the rate of surface-forced water mass transformation in the eastern SPG, the
 296 variability of the overturning circulation at 45°N, and ocean heat content trends in the SPG. The 5-year
 297 delay between surface property changes in the SPG and downstream circulation changes suggests good
 298 skills for short-term predictability in the region from the sole use of ocean surface and air-sea interface
 299 measurements. Here, a strong intensification of the overturning and associated heat transport from 2010
 300 is found to persist until the early 2020's, driving a new significant reversal of climatic condition in the
 301 SPG as temperature rapidly rise from their last minimum of 2017. The extreme winters of 2014 and 2015
 302 appear as key drivers of those recent and upcoming changes in the SPG. They are found to be responsible
 303 for rapidly cooling the upper ocean while feeding a 5-year delayed intensification of the overturning

304 through increased light-to-dense transformation, leading eventually to a sharp warming of the domain.
305 We note that the series of oceanic events described herein, from surface-forced water mass transformation
306 to meridional circulation and heat content changes, are only suggestively presented as a forced response
307 to atmospheric variability. Understanding the extent to which they may belong to a more complex loop
308 of coupled ocean-atmosphere interactions is beyond the scope of the present study. Finally, the present
309 analysis confirms the suitability of the international mooring-based OSNAP array for capturing the bulk
310 of interannual and decadal circulation changes driven by air-sea buoyancy exchanges in the whole
311 subpolar area.

312

313 **Acknowledgments**

314 DD and GM were supported by Ifremer. HM was supported by CNRS. ND was supported by University
315 of Brest. DD carried out the data analysis. This work was supported by the french national programme
316 LEFE/INSU: OBLADY and SOMOVAR, leaded by DD and GM, respectively. All authors contributed
317 to the interpretation, description and presentation of the results. All datasets used herein are available
318 online (see Supplementary Information for references).

319

320 **References**

321 Bersch, M., Yashayaev, I. and Koltermann, K. P.: Recent changes of the thermohaline circulation in the
322 subpolar North Atlantic, *Ocean Dyn.*, 57(3), 223–235, doi:10.1007/s10236-007-0104-7, 2007.

323 Bower, A. S., Lozier, M. S., Gary, S. F. and Böning, C. W.: Interior pathways of the North Atlantic
324 meridional overturning circulation, *Nature*, 459(7244), 243–247, doi:10.1038/nature07979, 2009.

325 Brambilla, E., Talley, L. D. and Robbins, P. E.: Subpolar mode water in the northeastern Atlantic: 2.
326 Origin and transformation, *J. Geophys. Res. Ocean.*, 113(4), 1–16, doi:10.1029/2006JC004063, 2008.

327 Bryden, H. L., King, B. A., McCarthy, G. D. and McDonagh, E. L.: Impact of a 30% reduction in Atlantic
328 meridional overturning during 2009-2010, *Ocean Sci.*, 10(4), 683–691, doi:10.5194/os-10-683-2014,
329 2014.

330 Buckley, M. W. and Marshall, J.: Observations, inferences, and mechanisms of the Atlantic Meridional
331 Overturning Circulation: A review, *Rev. Geophys.*, 54(1), 5–63, doi:10.1002/2015RG000493, 2016.

332 Curry, B., Lee, C. M. and Petrie, B.: Volume, Freshwater, and Heat Fluxes through Davis Strait, 2004–
333 05*, *J. Phys. Oceanogr.*, 41(3), 429–436, doi:10.1175/2010JPO4536.1, 2011.

334 Desbruyères, D., Mercier, H. and Thierry, V.: On the mechanisms behind decadal heat content changes
335 in the eastern subpolar gyre, *Prog. Oceanogr.*, 132, 262–272, doi:10.1016/j.pocean.2014.02.005, 2015.

336 Duchez, A., Frajka-Williams, E., Josey, S. A., Evans, D. G., Grist, J. P., Marsh, R., McCarthy, G. D.,
337 Sinha, B., Berry, D. I. and Hirschi, J. J.-M.: Drivers of exceptionally cold North Atlantic Ocean
338 temperatures and their link to the 2015 European heat wave, *Environ. Res. Lett.*, 11(7), doi:10.1088/1748-
339 9326/11/7/074004, 2016.

340 Gourcuff, C., Lherminier, P., Mercier, H. and Le Traon, P. Y.: Altimetry combined with hydrography for
341 ocean transport estimation, *J. Atmos. Ocean. Technol.*, 28(10), 1324–1337,
342 doi:10.1175/2011JTECHO818.1, 2011.

343 Grist, J. P., Marsh, R. and Josey, S. A.: On the Relationship between the North Atlantic Meridional
344 Overturning Circulation and the Surface-Forced Overturning Streamfunction, , 4989–5002,
345 doi:10.1175/2009JCLI2574.1, 2009.

346 Grist, J. P., Josey, S. A., Marsh, R., Good, S. A., Coward, A. C., De Cuevas, B. A., Alderson, S. G., New,
347 A. L. and Madec, G.: The roles of surface heat flux and ocean heat transport convergence in determining
348 Atlantic Ocean temperature variability, *Ocean Dyn.*, 60(4), 771–790, doi:10.1007/s10236-010-0292-4,
349 2010.

350 Grist, J. P., Josey, S. A., Marsh, R., Kwon, Y. O., Bingham, R. J. and Blaker, A. T.: The surface-forced
351 overturning of the North Atlantic: Estimates from modern era atmospheric reanalysis datasets, *J. Clim.*,
352 27(10), 3596–3618, doi:10.1175/JCLI-D-13-00070.1, 2014.

353 Hansen, B. and Østerhus, S.: North Atlantic-Nordic Seas exchanges, *Prog. Oceanogr.*, 45(2), 109–208,
354 doi:10.1016/S0079-6611(99)00052-X, 2000.

355 Hansen, B., Larsen, K. M. H., Hátún, H., Kristiansen, R., Mortensen, E. and Østerhus, S.: Transport of
356 volume, heat, and salt towards the Arctic in the Faroe Current 1993-2013, *Ocean Sci.*, 11(5), 743–757,

357 doi:10.5194/os-11-743-2015, 2015.

358 Josey, S. A., Hirschi, J. J.-M., Sinha, B., Duchez, A., Grist, J. P. and Marsh, R.: The Recent Atlantic Cold
359 Anomaly: Causes, Consequences, and Related Phenomena, *Ann. Rev. Mar. Sci.*, 10(1), 475–501,
360 doi:10.1146/annurev-marine-121916-063102, 2018.

361 Krauss, W.: The North Atlantic Current, *J. Geophys. Res.*, 91(C4), 5061–5074,
362 doi:10.1029/JC091iC04p05061, 1986.

363 Lherminier, P., Mercier, H., Huck, T., Gourcuff, C., Perez, F. F., Morin, P., Sarafanov, A. and Falina, A.:
364 The Atlantic Meridional Overturning Circulation and the subpolar gyre observed at the A25-OVIDE
365 section in June 2002 and 2004, *Deep. Res. Part I Oceanogr. Res. Pap.*, 57(11), 1374–1391,
366 doi:10.1016/j.dsr.2010.07.009, 2010.

367 Li, F., Lozier, M. S. and Johns, W. E.: Calculating the meridional volume, heat, and freshwater transports
368 from an observing system in the subpolar North Atlantic: Observing system simulation experiment, *J.*
369 *Atmos. Ocean. Technol.*, 34(7), 1483–1500, doi:10.1175/JTECH-D-16-0247.1, 2017.

370 Lozier, M. S., Bacon, S., Bower, A. S., Cunningham, S. A., De Jong, M. F., De Steur, L., De Young, B.,
371 Fischer, J., Gary, S. F., Greenan, B. J. W., Heimbmbach, P., Holliday, N. P., Houpert, L., Inall, M. E.,
372 Johns, W. E., Johnson, H. L., Karstensen, J., Li, F., Lin, X., Mackay, N., Marshall, D. P., Mercier, H.,
373 Myers, P. G., Pickart, R. S., Pillar, H. R., Straneo, F., Thierry, V., Weller, R. A., Williams, R. G., Wilson,
374 C., Yang, J., Zhao, J. and Zika, J. D.: Overturning in the Subpolar north Atlantic program: A new
375 international ocean observing system, *Bull. Am. Meteorol. Soc.*, 98(4), 737–752, doi:10.1175/BAMS-D-
376 16-0057.1, 2017.

377 Lozier, M. S., Li, F., Bacon, S., Bahr, F., Bower, A. S., Cunningham, S. A., de Jong, M. F., de Steur, L.,
378 deYoung, B., Fischer, J., Gary, S. F., Greenan, B. J. W., Holliday, N. P., Houk, A., Houpert, L., Inall, M.
379 E., Johns, W. E., Johnson, H. L., Johnson, C., Karstensen, J., Koman, G., Le Bras, I. A., Lin, X., Mackay,
380 N., Marshall, D. P., Mercier, H., Oltmanns, M., Pickart, R. S., Ramsey, A. L., Rayner, D., Straneo, F.,
381 Thierry, V., Torres, D. J., Williams, R. G., Wilson, C., Yang, J., Yashayaev, I. and Zhao, J.: A sea change
382 in our view of overturning in the subpolar North Atlantic, *Science (80-.)*, 363(6426), 516 LP – 521,
383 doi:10.1126/science.aau6592, 2019.

384 Marsh, R.: Recent variability of the North Atlantic thermohaline circulation inferred from surface heat
385 and freshwater fluxes, *J. Clim.*, 13(18), 3239–3260, doi:10.1175/1520-
386 0442(2000)013<3239:RVOTNA>2.0.CO;2, 2000.

387 Marsh, R., Josey, S. a., Nurser, a. J. G., de Cuevas, B. a. and Coward, a. C.: Water mass transformation
388 in the North Atlantic over 1985–2002 simulated in an eddy-permitting model, *Ocean Sci.*, 1, 127–144,
389 doi:10.5194/osd-2-63-2005, 2005.

390 Maze, G., Forget, G., Buckley, M., Marshall, J. and Cerovecki, I.: Using Transformation and Formation
391 Maps to Study the Role of Air–Sea Heat Fluxes in North Atlantic Eighteen Degree Water Formation, *J.*
392 *Phys. Oceanogr.*, 39(8), 1818–1835, doi:10.1175/2009JPO3985.1, 2009.

393 Mercier, H., Lherminier, P., Sarafanov, A., Gaillard, F., Daniault, N., Desbruyères, D., Falina, A., Ferron,
394 B., Gourcuff, C., Huck, T. and Thierry, V.: Variability of the meridional overturning circulation at the
395 Greenland-Portugal OVIDE section from 1993 to 2010, *Prog. Oceanogr.*, 132, 250–261,
396 doi:10.1016/j.pocean.2013.11.001, 2015.

397 Mertens, C., Rhein, M., Walter, M., Böning, Claus, W., Behrens, E., Kieke, D., Steinfeldt, R. and Stöber,
398 U.: Circulation and transports in the Newfoundland Basin, western subpolar North Atlantic, *J. Geophys.*
399 *Res. Ocean.*, 119, 7772–7793, doi:10.1002/2014JC010019.Received, 2014.

400 Pickart, R. S. and Spall, M. A.: Impact of Labrador Sea Convection on the North Atlantic Meridional
401 Overturning Circulation, *J. Phys. Oceanogr.*, 37(9), 2207–2227, doi:10.1175/JPO3178.1, 2007.

402 Piecuch, C. G., Ponte, R. M., Little, C. M., Buckley, M. W. and Fukumori, I.: Mechanisms underlying
403 recent decadal changes in subpolar North Atlantic Ocean heat content, *J. Geophys. Res. Ocean.*, (Figure
404 1), 1–17, doi:10.1002/2017JC012845, 2017.

405 Riser, S. C., Freeland, H. J., Roemmich, D., Wijffels, S., Troisi, A., Belbéoch, M., Gilbert, D., Xu, J.,
406 Poulouen, S., Thresher, A., Le Traon, P. Y., Maze, G., Klein, B., Ravichandran, M., Grant, F., Poulain,
407 P. M., Suga, T., Lim, B., Sterl, A., Sutton, P., Mork, K. A., Vélez-Belchí, P. J., Ansorge, I., King, B.,
408 Turton, J., Baringer, M. and Jayne, S. R.: Fifteen years of ocean observations with the global Argo array,
409 *Nat. Clim. Chang.*, 6(2), 145–153, doi:10.1038/nclimate2872, 2016.

410 Robson, J., Ortega, P. and Sutton, R.: A reversal of climatic trends in the North Atlantic since 2005, *Nat.*

411 Geosci., 9(7), 513–517, doi:10.1038/ngeo2727, 2016.

412 Robson, J., Polo, I., Hodson, D. L. R., Stevens, D. P. and Shaffrey, L. C.: Decadal prediction of the North
413 Atlantic subpolar gyre in the HiGEM high-resolution climate model, *Clim. Dyn.*, 50(3), 1–17,
414 doi:10.1007/s00382-017-3649-2, 2017.

415 Sarafanov, A., Falina, A., Mercier, H., Sokov, A., Lherminier, P., Gourcuff, C., Gladyshev, S., Gaillard,
416 F. and Daniault, N.: Mean full-depth summer circulation and transports at the northern periphery of the
417 Atlantic Ocean in the 2000s, *J. Geophys. Res. Ocean.*, 117(1), 1–22, doi:10.1029/2011JC007572, 2012.

418 Toole, J. M., Andres, M., Le Bras, I. A., Joyce, T. M. and McCartney, M. S.: Moored observations of the
419 Deep Western Boundary Current in the NW Atlantic: 2004-2014, *J. Geophys. Res. Ocean.*, 1–18,
420 doi:10.1002/2017JC012984, 2017.

421 Walin, G.: On the relation between sea-surface heat flow and thermal circulation in the ocean, *Tellus*,
422 34(2), 187–195, doi:10.3402/tellusa.v34i2.10801, 1982.

423 Wunsch, C.: What is the thermohaline circulation?, *Science (80-.)*, 298(November), 1179–81,
424 doi:10.1126/science.1079329, 2002.

425 Yashayaev, I. and Loder, J. W.: Further intensification of deep convection in the Labrador Sea in 2016,
426 *Geophys. Res. Lett.*, 44(3), 1429–1438, doi:10.1002/2016GL071668, 2017.

427 Zantopp, R., Fischer, J., Visbeck, M. and Karstensen, J.: From interannual to decadal: 17 years of
428 boundary current transports at the exit of the Labrador Sea, *J. Geophys. Res. Ocean.*, 1–25,
429 doi:10.1002/2016JC012271.Received, 2017.

430